Biosensors and Bioelectronics 126 (2019) 725–733

Contents lists available at ScienceDirect

Biosensors and Bioelectronics

journal homepage: www.elsevier.com/locate/bios

Bubble-free rapid microfluidic PCR

Sang Hun Lee[a,b], Jihwan Song[a,b,1], Byungrae Cho[a,b,c], SoonGweon Hong[a,b], Ori Hoxha[a,b], Taewook Kang[d], Dongchoul Kim[e], Luke P. Lee[a,b,c,f,g,*]

[a] Department of Bioengineering, University of California Berkeley, CA 94720, USA
[b] Berkeley Sensor and Actuator Center, University of California Berkeley, CA 94720, USA
[c] UC Berkeley and UCSF Joint Graduate Program in Bioengineering, Berkeley/San Francisco, USA
[d] Department of Chemical and Biomolecular Engineering, Sogang University, Seoul 121-742, Republic of Korea
[e] Department of Mechanical Engineering, Sogang University, Seoul 121-742, Republic of Korea
[f] Department of Electrical Engineering and Computer Science, University of California Berkeley, CA 94720, USA
[g] Biophysics Graduate Program, University of California Berkeley, CA 94720, USA

ARTICLE INFO

Keywords:
Nanoporous polymers
Polymerase chain reaction
Bubble-free microfluidic PCR
Molecular diagnosis
Lung cancer biomarker

ABSTRACT

Microfluidic polymerase chain reaction (PCR) has been of great interest owing to its ability to perform rapid and specific nucleic acid amplification and analysis on small volumes of samples. One of the major drawbacks of microfluidic PCR is bubble generation and reagent evaporation, which can cause malfunctions. Here, through theoretical modeling and characterization of bubble behavior, we propose a bubble-free microfluidic PCR device via controlled fluid transfer. Our approach exploits a thin impermeable polyethylene (PE) top layer that minimizes the generation of bubbles by inhibiting mass transport along a vertical direction. Simulation results demonstrate that a calculated mass flow difference of approximately 370% can be obtained by utilizing an impermeable membrane as the vertical barrier layer. To demonstrate proof-of-concept, two nanoporous polymeric materials, poly(dimethylsiloxane) (PDMS) and PE, were used for stand-alone self-powered sample loading (approximately 70 s) and for use as a vertical barrier layer, respectively. Consequently, we demonstrate successful amplification of the cMET gene, a nucleic acid (NA) biomarker for lung cancer, and complete an ultrafast PCR test in less than 3 min using a high powered Peltier-based thermal cycler under bubble-free conditions. This approach will result in a new paradigm for ultrafast molecular diagnosis and can facilitate NA-based nearly instantaneous diagnostics for point-of-care testing and for personalized and preventive medicine.

1. Introduction

The gold standard for the quantitative diagnosis of diseases is divided into two main categories: polymerase chain reaction (PCR) for nucleic acid (NA) biomarkers and immunoassay-based methods for protein biomarkers (Lee et al., 2012; Ma et al., 2018; Rissin et al., 2010; Ueberfeld et al., 2008). In particular, PCR is widely used as a molecular diagnostic technique to amplify copies of specific fragments of DNA using temperature cycling. In particular, molecular diagnosis tool-based rapid diagnostics can be used to reduce to delay in cancer biomarker analyses and related treatment choices for a patient who has metastatic cancer with acute deterioration. Also, various cancer biomarkers such as *cMET, BRAF,* and *NRAS* gene are linked to metastatic progression and are viable targets for a significant subset of advanced stage of cancer (Park et al., 2016). Thus, the rapid determination of metastatic cancer's mutation status is now a major criterion for treatment choices. However, conventional PCR methods require the use of specialized instruments for thermal cycling and trained personnel to complete the assays. Therefore, many researchers have tried to improve thermal cycling time and PCR efficiency/yield (Farrar and Wittwer, 2015). Even though many commercial PCR systems have been improved in the performance such as the average ramp rate and throughput as shown in the Table S1, there are still drawback, for instance, if the commercial thermal cyclers are run at full capacity of 96 well format, it would take over 1 h/single PCR assay. Also, conventional bulky PCR instruments are not suitable for point-of-care testing (POCT) in resource-limited environments such as developing countries due to high power consumption, typical plate (96/386 wells) or tube-based assay format and need of trained personnel (Liu et al., 2017). By contrast, microfluidic PCR offers many advantages over conventional PCR procedures, including lower

* Corresponding author at: Department of Bioengineering, University of California Berkeley, CA 94720, USA.
E-mail address: lplee@berkeley.edu (L.P. Lee).
[1] Present address: Department of mechanical engineering, Hanbat National University, Daejeon 34158, Republic of Korea.

https://doi.org/10.1016/j.bios.2018.10.005
Received 17 June 2018; Received in revised form 3 October 2018; Accepted 3 October 2018
Available online 11 October 2018
0956-5663/

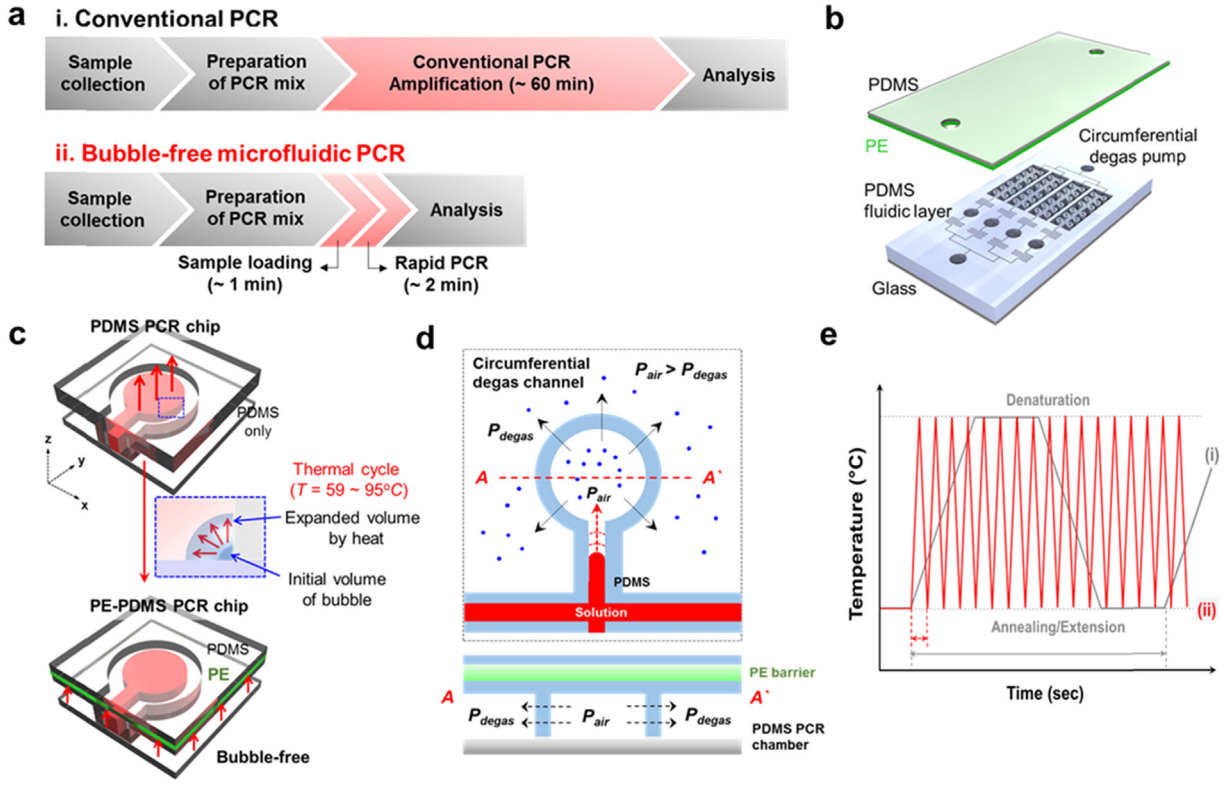

Fig. 1. Schematic illustration of a bubble-free microfluidic PCR chip. (a) Comparison of convention-al benchtop and microfluidic PCR for rapid nucleic acid diagnostics, (b) Schematic illustration of a bubble-free microfluidic PCR device embedded in polyethylene (PE) barrier layer for reliable PCR reaction. This microfluidic PCR chip consists of a PCR chamber (500 μm in diameter and 100 μm in height), and a polymer layer for bubble-free PCR. (c) Principle of a PE barrier on a microfluidic PCR device. To prevent the loss of PCR fluids by the liquid/gas diffusion through PDMS, the PE barrier layer was spin-coated. (d) Schematic illustration of stand-alone sample loading in a hybrid PE-PDMS PCR chip. Degas-driven flow is generated when the PCR chip is changed to an atmospheric pressure from a low pressure environment. The circumferential degas channel can accelerate the suction flow rate up to 6-fold. A-A indicates the cross-sectional view in the bottom side figure, (e) Comparison of temperature profiles. i) and ii) represent the benchtop and Peltier-based thermal cycles, respectively.

consumption of reagents and biological samples (lower cost/test), higher single-molecule detection efficiency in a reduced reaction volume, shortened analysis time through faster cycling, and portability and automation for use by minimally trained personnel (Hung et al., 2017; Sayad et al., 2018). Thus, substantial efforts have been made to improve the speed and performance of microfluidic PCR methods that have been used in many diagnostic and research fields, such as virus detection, disease-associated NA detection, genetic disease diagnostics, evolutionary biology, agriculture R&D and industry, and food safety testing (Heyries et al., 2011; Jiang et al., 2014; Liao et al., 2005; Liao et al., 2013; Maltezos et al., 2008).

In spite of the many advantages of microfluidic PCR, there are still many challenges to overcome in developing an efficient microfluidic PCR device. The major drawbacks of microfluidic PCR are bubble formation, non-specific adsorption of biological samples and integration of microfluidic components, such as micro-pumps, valves and mixers on a microfluidic PCR platform (Zhang and Xing, 2007; Zhang et al., 2006). In particular, regarding bubble formation, air trapped in the reaction chamber can expand at high temperatures and lead to sample evaporation, a temperature drop, and expulsion of the PCR solution out of the reaction chamber (Karlsson et al., 2013; Nakayama et al., 2010; Prakash et al., 2006). In particular, the evaporation of PCR reagent during thermal cycles is significant problem, when the temperature approaches 95 °C at the denaturation step. The air bubble in the PCR chamber can expand quickly, accompanied with increasing pressure, then it can purge the PCR reagent out of the PCR chamber which can accelerate the evaporation. This cascade related to the evaporation is critical for loss of PCR reagents in concentration and volume of PCR solution because of the small sample volume and large surface-to-volume ratio of microfluidic device. Previous bubble removal approaches in microfluidic PCR utilized porous structures, membranes, and implanting of parylene, poly(vinyl alcohol), Teflon, and polyethylene (PE), which also used for the same purpose in our study (Liu et al., 2007; Shin et al., 2003; Xu et al., 2010). Therefore, these problems must be controlled carefully during thermal cycling to facilitate NA amplification in the most effective manner. Thus, for potential and practical applications, many critical aspects must be considered and improved to produce an efficient microfluidic PCR, including 1) a micro-machining technology for use with substrate materials, fabrication, bonding and sealing, 2) design parameters, such as the architecture of PCR reaction chambers regarding the handling of sample fluids, including flow-through/stationary PCR chamber formats, and 3) analytical and signal processing methods for detection of amplicons and the integration of these methods with other functional units, such as a sample preparation, miniaturized thermal cycler, and detection module to construct the POCT device (Almassian et al., 2013).

Here, we report the design, theoretical analysis, fabrication and characterization of bubble-free microfluidic PCR devices for potential applications in the POC molecular diagnostics. Theoretical modeling, in addition to consideration of the design parameters of PCR chambers for bubble-free PCR in a confined microfluidic environment, was conducted to ensure a bubble-free environment in a microfluidic PCR reaction. Based on the theoretical analysis, we designed and fabricated bubble-free microfluidic PCR devices with two different types of polymeric materials, poly(dimethylsiloxane) (PDMS) and polyethylene (PE) with two different functionalities: 1) the high-gas solubility of PDMS for stand-alone bubble-free sample loading, and 2) the liquid/gas barrier property of PE for a bubble-free environment during the PCR reaction

along with a fabrication convenience. In this study, we assume that the generation of bubble inside PCR chamber due to the absorption of water by porous PDMS, could accelerate the liquid loss through bubble expansion, accompanied with increasing pressure during rapid microfluidic PCR process. In addition, we designed our microfluidic PCR chamber with surrounding the circumferential degas channel, which can achieve the guided-bubble escape, reducing the pressure inside the PCR chamber. To construct rapid NA detection module, we established a rapid bubble-free microfluidic PCR platform combined with an ultrafast Peltier-based thermal cycler as described in Fig. 1. With our diagnostic platform, successful amplification of *cMET*, a lung cancer biomarker gene of non-small cell lung cancer (NSCLC), was demonstrated without bubble formation and sample evaporation in a run time of approximately 3 min.

2. Materials and methods

2.1. Materials and equipment

Trizol, a Superscript cDNA synthesis kit, E-gel (2% with SYBR Safe DNA gel) were purchased from Invitrogen (USA). Polyethylene and BSA were obtained from Sigma Aldrich (USA). PDMS (Sylgard 184), cMET TaqMan probe, Cyxi Fast PCR mix, and glass slide were obtained from Dow Corning (USA), Applied Biosystems (USA), Fluorogenics (UK), and Thermo Scientific (USA), respectively. Photolithography film masks were purchased from Fineline Imaging, Inc (USA). Peltier (VT-199–1.4-0.8, TE Technology, Inc., USA), thermocouple-type K (Omega Engineering, Inc, USA), Arduino Uno (Arduino, Italy), a thermocouple amplifier (MAX31855, Adafruit, USA) were used to construct the miniaturized thermal cycler. The NSCLC cell line (HCC-1975) was gifted from Prof. Sanjiv S. Gambhir (School of Medicine, Stanford University). E-gel safe transilluminator (Invitrogen, USA), nanodrop spectrophotometer (Thermo Scientific, USA), real-time benchtop thermocycler (CFX96, Bio-Rad, USA), a fluorescent microscope (Nikon, Japan) with a CCD camera were used for the experiment.

2.2. Bubble-free microfluidic PCR device fabrication

The microfluidic PCR device was fabricated using PDMS by standard soft lithographic techniques. To control the geometry of microfluidic PCR device, we designed the different version of transparent 2D photomasks. We fabricated a bubble-free microfluidic PCR chip with a polymer layer that functioned as a vertical liquid/gas barrier layer. The PCR chip consists of two layers of PDMS. The bottom layer is for making a fluidic layer with PCR reaction chambers, while the top layer prevents evaporation by holding the polyethylene film securely in place. PDMS (Sylgard 184, Dow Corning) was prepared using a 1:10 ratio of cross-linker to base. A constant amount of the PDMS mixture was poured into a mold to create PDMS chips of constant thickness (1 mm) for fabrication of the PCR devices with a flow layer. After curing the first PDMS channel layer for at least 4 h at 80 °C, a 3% (w/v) solution of PE in toluene was spin-coated over the PCR channel at 200 rpm to prevent the vertical evaporation of sample fluid. To control the gas permeability of the PE layer, more PE (> 3% w/v of PE) could be used in the spin-coating process. Then, an additional PDMS layer was added to obtain the hybrid PE-PDMS layer. The PDMS was removed from the mold and then punched with a 1 mm outer diameter puncher to form a sample inlet. The PCR chamber was 500 μm in diameter and 100 μm in height (approximately 20 nL in a single PCR chamber). After 30 s of plasma treatment (20 W, 30 s, 0.2 Torr, PE-1000, RF Generator, Advanced Energy. Inc.), the PCR chip was bonded on a glass slide (22 × 40 × 0.17 mm glass, No. 1, Fisher Scientific) to prevent the pressure on the bonding interface from expanding liquid/gas during thermal cycles. Image J (NIH) was used to calculate the liquid/gas ratio in the PCR chambers based on the images taken in the experiments.

2.3. Peltier-based miniaturized thermal cycler fabrication

The prototype rapid PCR thermal cycler consisted mainly of a Peltier thermoelectric cooler, heat sink and thermal controller. A heat sink block was used to maintain one side of the thermoelectric cooler at room temperature, while the other side of the thermoelectric cooler functions as a thermal cycler. Attaching a diced silicon wafer to the surface of the thermal cycler ensured the uniformity of temperature. The dimensions of the thermal cycler unit are approximately 20 × 20 × 5 mm. A programmable thermal controller was assembled using an Arduino Uno microcontroller, type K thermocouple, and a thermocouple amplifier, MAX31855. The thermocouple was attached to the surface of the thermal cycler to measure the temperature for closed-loop control. The thermal controller recorded the temperature and time sequences in real-time for later analysis. The production cost for the disposable chip with a low complexity is less than $10 and can be further reduced when mass-produced by the injection molding (< $0.4) (Boone et al., 2002; Yeh et al., 2017). The equipment cost regarding the miniaturized rapid thermal cycler setup is estimated to be about < $110 as shown in Table S2.

2.4. Preparation of cDNA and PCR amplification

The fabricated device was used for rapid PCR involving cDNA samples from HCC-1975, a non-small cell lung cancer cell line (NSCLC). Total RNA was extracted from HCC-1975 cells at 1×10^6 cells/ml using a TRIzol reagent (Invitrogen). The concentration of RNA samples was determined using a NanoDrop spectrophotometer (Thermo Scientific) by measuring the absorbance at 260 nm. The extracted total RNA was used to synthesize cDNA using a Superscript cDNA synthesis kit (Invitrogen) with oligo (dT) primers. Briefly, 500 ng of total RNA was used as a starting material, and the mixture containing RNA, oligo (dT), and dNTPs, was heated at 65 °C for 5 min and then at 45 °C for 15 min. The reaction was inactivated at 95 °C for 2 min.

Copy number (C, copies/μl) for the *cMET* template was calculated as follows: $C = P{\cdot}A/G{\cdot}M{\cdot}X$, where P is the PCR product concentration (ng/μl), A is Avogadro's constant (6×10^{23}), G is the amplicon size (bp), M is the multiplying constant (1×10^9) and X is the average molecular weight of the 1 bp in the amplicon (650 Da) (Xu et al., 2015). Template DNA was serially diluted from 10^2 to 10^6 copies and was used as a template in the PCR assay. To calculate the limit of detection (LOD) per single well, the initial copy number was converted as follows: For instance, a 5 μl of cDNA with a concentration of the 1.5×10^4 copies/μl was diluted into a PCR master mix of 20 μl volume. The final concentration of the copy number is 7.5×10^4 copies/20 μl, which is equivalent to a concentration of 3.75×10^3 copies/1 μl (≈ 3.75 copies/1 nl). We converted this value to copies of target DNA/single well. Thus, the copy number/single well can be calculated by multiplying 20 to the final concentration per 1 nl since the volume of PCR chamber was calculated to be 20 nl/well. In this research, the TaqMan probe for *cMET* (assay ID: Hs01565584-m1, Applied Biosystems, RefSeq: NM_000245.2, see the Fig. S2) was used for the detection of the amplicon (the length of the amplicon: 89 bp).

For the benchtop PCR, a 20 μl PCR mixture consisted of 10 μl of Cyxi Fast PCR master mix (Fluorogenics), 5 μl of cDNA template (7.5×10^4 copies/total 20 μl, final conc.: 3.75 copies/1 nl) and 1 μl of TaqMan probe (a range of 250–1000 nM was used in optimization studies). The 1 μl of bovine serum albumin (BSA, 20% w/v stock solution) was used in the PCR mix to stabilize the polymerase and to reduce undesired adsorption of polymerase onto the inner surface of the PDMS channel (Zhang et al., 2006). Then 3 μl of water was added to bring the final volume to 20 μl. The thermal cycling protocol was 35 cycles of 94 °C for 1 s, and 59 °C for 1 s using the benchtop thermocycler (Minimum hold time: 1 s, Bio-Rad C1000 thermal cycler with CFX96 real-time PCR detection system). After the benchtop PCR amplification as a reference PCR, the amplicon was visualized by 2% agarose gel (E-Gel 2% with

SYBR Safe DNA gel stain, 50 bp DNA ladder, Invitrogen). A gel image was taken with an E-gel Safe Imager Transilluminator.

For the microfluidic PCR, 3 μl of the PCR mixture, ensuring that no dead-volume in the inlet were loaded into a bubble-free microfluidic PCR device by a degas-driven flow. To increase the amplification efficiency in the rapid microfluidic PCR, the optimized concentrations of probes and polymerases were used. The PCR for the microfluidic PCR was performed using the following PCR mixture: 10 μl of 2.5x Cyxi Fast PCR master mix (2.5 units of polymerase), 5 μl of cDNA template, 1 μl of TaqMan probe, 1 μl of bovine serum albumin (BSA, 20% w/v stock solution) and 3 μl of water. The negative control was made using the same PCR mixture as the other samples by replacing 5 μl of water instead of cDNA template. The rapid thermal cycle conditions were 94 °C for 0 s, and 59 °C for 0 s for a total of 35 cycles with no hold time at each denaturation/annealing step. After the microfluidic PCR amplification, the fluorescent intensity of PCR product from a single PCR well was analyzed by Image J (NIH) with the images taken in the microfluidic PCR experiment. The analytical performance of microfluidic PCR amplification was determined through the end-point fluorescent analysis via epi-fluorescence microscopy. The limits of detection and quantification were calculated by the relationship between the standard deviation (*SD*) of the calibration curve and its slop (*S*) (Bustin et al., 2009; Shrivastava and Gupta, 2011). The limits of detection and quantification were calculated from the following equations: LOD = 3 *SD/S* and LOQ = *10 SD/S*.

3. Result and discussion

3.1. Design concept for bubble-free microfluidic PCR

We report the design, fabrication and characterization of bubble-free microfluidic PCR devices. Thus, we focused on the bubble suppression-associated design of the PCR chamber for efficient bubble-free microfluidic PCR, considering a low-permeable vertical barrier layer, the geometry of the PCR chamber and the side wall thickness. A conceptual basis of the rapid microfluidic PCR platform for the POC diagnostic system is described in Fig. 1a. We employ rapid stand-alone sample loading (~1 min) and thermal cycling (~2 min). Consequently, the total run time was shortened up to 20-fold while ensuring rapidity and reliability, compared to the run-time from the commercial benchtop PCR cycler under standard PCR protocol. Fig. 1b shows a schematic illustration for a microfluidic PCR chip. In this study, two different types of polymers, PDMS and PE, were used to make hybrid structures with a different functionality on microfluidic PCR devices. The bubble-free microfluidic PCR chip consists of a PDMS fluidic layer containing the ring-shaped dead-end PCR reaction chambers and circumferential degas channels and a PE-based liquid/gas barrier layer over the PDMS fluidic layer. In particular, PE was used to ensure a more reliable PCR by suppressing fluid loss by evaporation and bubble generation, overcoming one of the major reasons for microfluidic PCR failure (Fig. 1c). By contrast, the high porosity of PDMS was advantageous for stand-alone sample loading by degas-driven flow without any external pump and flow control (Liu et al., 2015). Our stand-alone sample loading concept aims to minimize the number of microfluidic components and to perform simple-to-use operation in resource-limited environment towards POC molecular diagnostics. Also, a vacuum sealed packing of the microfluidic PCR device is beneficial for 'ready for use' by ensuring good long-term storage conditions (Dimov et al., 2011). The mechanism of fluid actuation by the degas-driven flow is described in Fig. 1d. We harness the high gas solubility of PDMS for fluid actuation. Flow force within the PDMS-based microfluidic PCR device could be stored as vacuum energy by degassing of the PDMS device for a certain period of time under a low-pressure environment. Once the degassed PDMS is brought into contact with atmospheric pressure, the pressure difference between the outside PDMS under atmospheric pressure and the inside of the dead-end PCR chamber drives the reabsorption of air into the dead-end PCR chamber which is a vacuum source. Thus, when the PCR sample completely seals the inlet of degassed microfluidic PCR device in atmospheric pressure, the pressure gradient withdraws the PCR sample into the dead-end PCR chamber as the free volume of the PDMS refills with the liquid, reducing the internal pressure in the microchannel (Xu et al., 2015). The PCR chambers can fill rapidly with PCR solution while the gas is being sucked through the ring-shaped thin PDMS side-wall to the circumferential degas channel by diffusion of the gas. Fig. 1e describes a comparison of the temperature profiles for single thermal cycles in both conventional and rapid thermal cyclers. The thermal ramp rate together with the amplification speed of current polymerases is a major limiting factor in PCR-based diagnostics. In this respect, the rapid thermal cycling system exhibited high ramp rates compared with the slower thermal ramp rates of the benchtop thermal cycler. Consequently, all our approaches presented here provide a significant improvement for the ultrafast NA diagnostic platform.

3.2. Theoretical principle of a bubble-free microfluidic PCR device

In the process of sample loading into microfluidic device, micro bubbles can be generated at the bonding interface and inner corners of the micro-chamber in the chip inside. For the numerical simulations, we assume that the generation of bubble inside PCR chamber due to the absorption of water by porous PDMS (Blume et al., 1991) could accelerate the liquid loss through bubble expansion during PCR process. The pressure is related to the thermal expansion of air through heat transfer (i.e., $\Delta V = \beta_{air} V \Delta T$) and bulk modulus (i.e., $\Delta P = -K\Delta V/V$). Therefore, the pressure, which changes according to the variation of temperature, can be obtained using the following equation: $\Delta P = -K\beta_{air}\Delta T$, where V, β_{air}, T, P, and K are volume of air bubble, thermal expansion coefficient of air (at 25 °C), temperature, pressure and bulk modulus of air, respectively. We did not consider the deformation of the PDMS because the thermal expansion coefficient of PDMS (i.e., 3.1×10^{-4} (1/K)) was 10 times less than that of the air (3.4×10^{-3} (1/K)). As the temperature increases ranging from 35 °C to 95 °C with 10 °C intervals, the pressure difference with atmospheric pressure, denoted as ΔP, is calculated to be 3.40, 6.80, 10.20, 13.60, 17.00, 20.40, and 23.46 kPa for each temperature, respectively. As the temperature increases, the exerted pressure in the PCR chamber caused by the expanded bubbles generates a flow of PCR solution through the permeable PDMS. To calculate the motion of fluid flow, the Navier-Stokes equation is used, and the fluid flow is assumed to be laminar, steady, viscous and incompressible. On the other hand, we treat the permeable PDMS as a porous medium. Thus, the Brinkman equation, which describes the flow in a porous medium, is adopted for use in the PDMS. A continuity equation is also considered with the above equations. Governing equations are as follows:

$$\rho\left(\frac{\partial \mathbf{u}}{\partial t} + \mathbf{u}\cdot\nabla\mathbf{u}\right) = -\nabla P + \mu(\nabla^2\mathbf{u}), \tag{1}$$

$$\frac{\rho}{\varepsilon_p}\left(\frac{\partial \mathbf{u}}{\partial t}\right) + \frac{\mu}{k}\mathbf{u} = -\nabla P + \frac{\mu}{\varepsilon_p}(\nabla^2\mathbf{u}), \tag{2}$$

$$\nabla\cdot\mathbf{u} = 0, \tag{3}$$

where ρ, *u*, *μ*, *εp*, and k denote the density of fluid, the velocity field of fluid, the dynamic viscosity, the porosity and the permeability of the porous medium, respectively.

To analyze bubble-free behavior, numerical simulations are performed using commercial software (COMSOL Multiphysics 4.4; Comsol, Inc.). In the simulation, the domain for the PCR chamber is constructed to be 500 μm in diameter (*D*) and 100 μm in height (*H*). The PCR chamber is enclosed by a thin PDMS side wall (t_{side}) with a thickness of 150 μm, and the thickness of the low permeable membrane (t_{top}) on the top side over the PDMS fluidic layer is set to 50 μm (Fig. 2a).

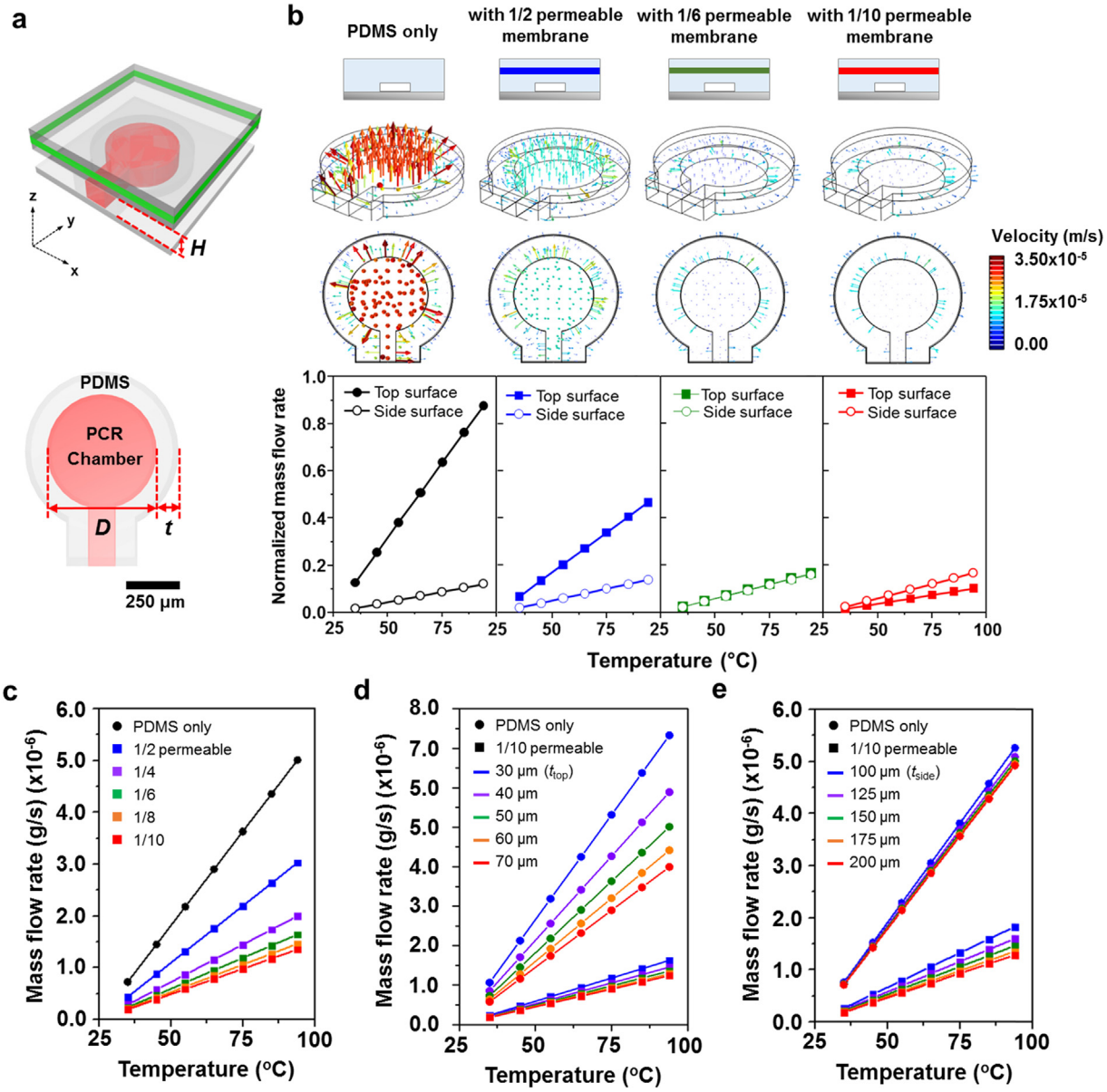

Fig. 2. Computational simulation of reduced permeability-driven bubble-free microfluidic PCR devices. (a) Schematic illustration of a simulation domain, (b) The velocity profiles of PCR fluids. Mass flow rate of PCR fluids through the top and side walls with respect to the permeability. The vertical liquid/gas barrier layers with the different permeability were embedded. The temperature of the bottom heater was set ranging from 30 to 95 °C and the top to 25 °C. (c) Comparison of total mass flow rates of PCR fluids with different permeable membranes. (d) Mass flow rate of PCR fluids in the PDMS chamber with the different thicknesses of the top layer (t_{top}), which was embedded the lowest permeable membrane (1/10 of PDMS). (e) Mass flow rate of PCR fluids in the PDMS chamber with the lowest permeable membrane (1/10 of PDMS) at different thicknesses of the side walls (t_{side}).

Fig. 2b represents the velocity profiles of outgoing molecules from the PCR chamber at the different lower temperatures ranging from 25 to 95 °C. The arrows are proportional to the velocities of the outgoing molecules. The mass flow rates were diminished as the permeable membranes were varied. To better clarify the effect of embedded barrier membranes, the mass flow rates of PCR fluids through the top and side walls were analyzed using membranes with varied permeability. The mass flow rates normalized with that of PDMS-only devices are denoted by the flow directions to the top and side walls. For a PDMS-only device, the ratio of mass flow rate between the top (filled rectangle) and side (open circle) directions shows that the loss of PCR fluid in the upward direction is dominant. Interestingly, the ratio is reversed at the embedded barrier layer with a 1/10 lower permeability.

It is noteworthy that the loss of PCR fluid in the confined microfluidic space can be improved when controlling the design parameters of PCR chambers, such as the thickness of top barrier layer (t_{top})/the side wall (t_{side}) and the aspect ratio of height and diameter of the PCR chamber. Fig. 2c shows the total mass flow rate for embedded barrier membranes with different permeabilities of (6.0, 7.5, 10, 15, and 30 nm^2). These values are reasonable, as the permeability of lower permeable polymers, such as Teflon, are within this range (Merkel et al., 2000). The increase in pressure triggered from the bubble expansion is applied at the inner corners of the PCR chamber. The chambers with much lower permeable membranes than PDMS (60 nm^2) show less fluid flow and smaller velocities compared to PDMS-only devices. The differences of mass flow rates in the absence/presence of lower permeable membranes gradually increased as the temperature increased. At the denaturation temperature in particular, the distinction of mass flow rate reached approximately 370%. A higher mass flow rate, which means a larger fluid loss in the PCR chamber, creates more

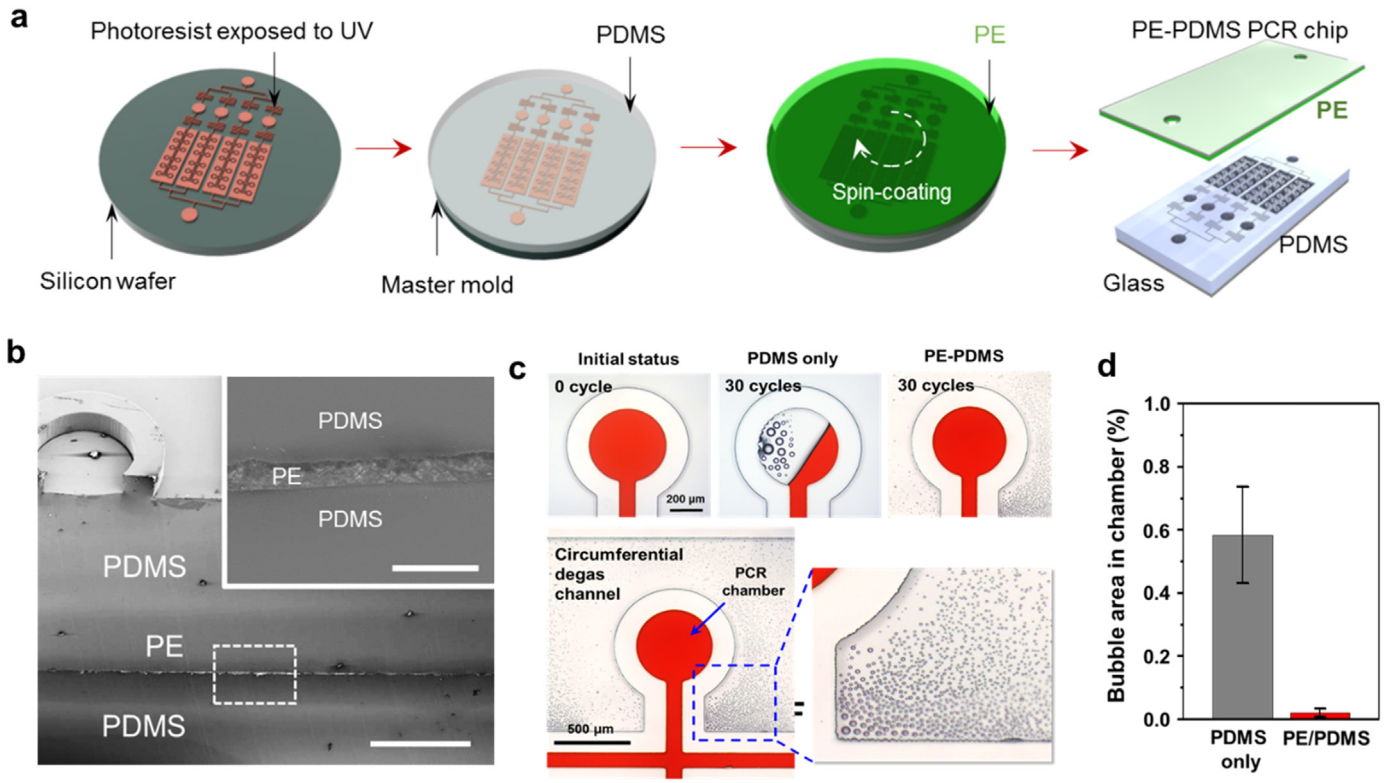

Fig. 3. Characterization of the bubble-free function of microfluidic PCR device. (a) Fabrication procedure for a bubble-free microfluidic PCR device. A PE barrier layer was spin-coated at 200 rpm for 30 s (b) SEM images of cross-sectional views for an embedded PE barrier layer. The scale bar represents 500 μm, 20 μm for in inset. (c) Bubble formation within a microfluidic PCR device after 30 cycles. In the middle of the photos, the bubbles inside the PDMS-only device were generated without a PE barrier layer. (d) Ratio of liquid/gas between a PDMS-only device and a PE-PDMS device after 30 cycles. (mean ± sd, N = 7).

favorable conditions for growing bubbles by their expansion. Thus, the bubble-free environment in the confined microfluidic space can be achieved by providing harsh conditions against the development of sustainable bubbles. As for other design parameters of the PCR chamber, we evaluated the effect of top barrier layer thickness (t_{top}) and side wall thickness (t_{side}) on the transport of liquid/gas in Fig. 2d and e. As shown in Fig. 2d, the mass flow rates at the different thickness of top barrier layer, embedded the 1/10 low permeable material were similar by inhibiting the mass flow along with a vertical direction. Apparently, the liquid/gas transport in this architecture was significantly reduced in the presence of top barrier layer regardless of the thickness of top layer in comparison with the PDMS-only device. As mentioned previously, the loss of PCR fluid was sufficiently diminished by utilizing a 1/10 permeable membrane, and the side wall of the PCR chamber could function as a horizontal resistance layer to reduce more transport of liquid/gas molecules as shown in Fig. 2e. As expected, by increasing the thickness of the side wall, the mass flow rate was decreased. It is resulted from that the PDMS-only device has the upward-dominant transport while the PDMS device embedded with 1/10 permeable membrane has a dominant mass flow along the side wall.

Based on our simulation results, we can suggest a design for the PCR chamber. The mass flow rate from manipulating the aspect ratio (diameter, *D*; height, *H*) was analyzed as shown in Fig. S1, where the volume of the chamber is constant in all cases. In the absence of a barrier layer (PDMS-only), the mass flow rate decreases as the aspect ratio decreases, because the total surface area of the PCR chamber decreases. However, regardless of the aspect ratio, the mass flow rate of the PCR chamber embedded with a 1/10 permeable membrane shows almost no change. Thus, to achieve a bubble-free environment, the design with a lower aspect ratio is better in a PDMS-only device as shown in Fig. S1c. On the other hand, a thick side wall is also effective in the presence of a low permeable membrane over the PCR chamber.

3.3. Characterization of bubble-free microfluidic PCR device

We were able to fabricate a bubble-free microfluidic PCR chip with a PE based barrier layer which functioned as a vertical liquid/gas barrier layer, as shown in Fig. 3a. PE has a low permeability to water and gas, approximately 100 times lower than that of PDMS (Prakash et al., 2006). Fig. 3b shows SEM images of cross-sections of bubble-free microfluidic PCR devices. The thickness of an embedded PE layer sandwiched between PDMS layers was approximately 10 μm. Fig. 3c and d depict the effect of a PE barrier layer on the bubble-free microfluidic PCR device. Red colored ink was used to provide better visualization. After 30 thermal cycles, the PE-PDMS structure maintained a bubble-free chamber, while a PDMS-only device exhibited bubble formation. The liquid bubbles as observed in the bottom image of Fig. 3c resulted from the PCR solution loss, matching the assumption that the PCR solution in the circumferential degas channel can be easily evaporated and condensed during the repeated heating and cooling of PCR. We speculate that the transport of water/vapor molecules through the PDMS sidewall was caused by the pressure gradient between the PCR chamber and the circumferential degas chamber. In the absence of the PE layer, over half of the fluid volume in the PCR chamber was lost after 30 thermal cycles, as shown in Fig. 3d. Consequentially, neither bubble formation nor reagent evaporation occurred in the PE-PDMS PCR device. In addition, the proposed PE-PDMS hybrid structure offers a reliable bubble-free PCR as well as a uniform heat distribution without a temperature drop triggered by bubble generation. These results show that our approach is effective in suppressing bubble formation and fluid loss during thermal cycles. When using the PE-PDMS device, the loss of PCR fluid from the PCR chamber into the circumferential degas channel is also expected to be at least 1.0% of total PCR fluid. The PCR solution can be easily evaporated and condensed, when it encounters the repeated heating and cooling in the circumferential degas channel filled

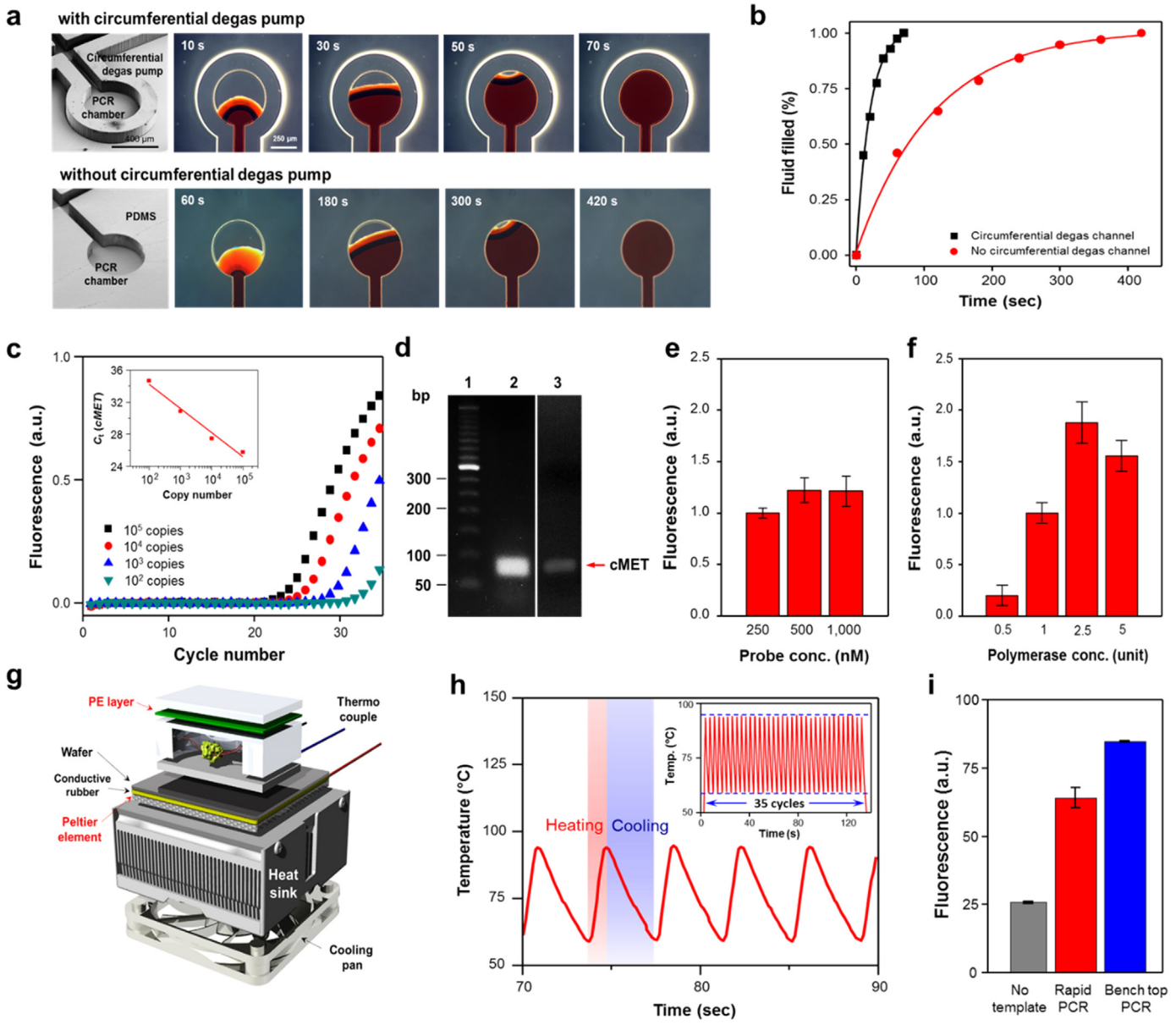

Fig. 4. Amplification of cMET using bubble-free microfluidic PCR. (a) Stand-alone sample loading with and without a circumferential degas channel at same degassing times. An image was taken every 10 s (b) Comparison of sample loading rates. (c) Calibration curve of the cMET gene at different initial concentrations of cDNA in the benchtop thermal cycler. (d) Agarose gel electrophoresis showing cMET gene amplification. Lanes 1, 2 and 3 are a low molecular weight DNA ladder, an amplicon for cMET from the benchtop PCR and rapid microfluidic PCR, respectively. The fluorescence intensity at different concentrations of TaqMan probe (e) and polymerase (f). (g) Schematic illustration of rapid bubble-free microfluidic PCR setup. A Peltier-based thermal cycler system runs one thermal cycle in approximately 3.7 s and completes a 35-cycle PCR in 2 min 10 s (h) Temperature profiles of Peltier-based rapid thermal cyclers. These data were recorded with a thermocouple. (i) The fluorescence signals from rapid microfluidic PCR and benchtop PCR at a concentration of 3.75×10^3 copies/μl of cDNA. A channel inlet was sealed with PCR tape on the top layer after the loading of 3 μl PCR fluid by degas-driven flow. The signal of 'no template' test was obtained from the microfluidic PCR test.

with air (Zhang et al., 2006). As a result, the loss of PCR solution only exists as liquid bubbles in the circumferential degas chamber. The phenomena presented here rely on the transport of liquid/gas through the ring-shaped thin PDMS side wall from the PCR chamber into the circumferential degas channel. Consequently, the functions of the circumferential degas channel are suitable for rapid degas-driven sample loading by providing an additional vacuum source as well as the control of bubble formation via the guided-bubble escapement.

3.4. Rapid PCR-based diagnosis for a NA biomarker

As mentioned above, our sample loading method relies on the high gas solubility of PDMS due to its intrinsic porosity (Merkel et al., 2000). A fluidic actuation force within the microfluidic PCR device was generated by degassing in a low-pressure environment. We designed two types of PCR chambers in the presence/absence of circumferential degas channels, as shown in the SEM images of Fig. 4a. The PCR fluid was loaded which then moved along the flow channel by degas-driven flow. Entire PCR chambers were completely filled with PCR fluid. In the case of the ring-shaped PCR chamber, a high flow rate was generated most of the time, however, the flow was decreased for a short time at the end of the sample loading process. No trapped air bubbles in the microscopic observation remained in the PCR chambers. Fig. 4b depicts the sample loading rate analyzed from time lapse images. The air from the PCR chamber easily seeped out into the neighboring circumferential channel during the suction process. After the sample loading, the

circumferential degas chamber was filled with air. As a result, the sample loading rate was enhanced up to 6-fold (approximately 70 s) in the presence of the circumferential degas channel compared with that with no circumferential degas channel.

An amplification of *cMET,* a lung cancer-associated NA marker for non-small cell lung cancer (NSCLC), was performed to verify the bubble-free microfluidic PCR platform. For a control, we carried out off-chip tests utilizing a conventional benchtop thermal cycler as shown in Fig. 4c-f. The benchtop qPCR detected low levels at the detection limit ($\sim 10^3$ template copies of cDNA in 35 cycles in terms of Ct value) as shown in Fig. 4c. The low amplification efficiency was attributed to rapid PCR protocol (95 °C for 1 s and 59 °C for 1 s in 35 PCR cycles, two-step protocol). The corresponding *cMET* gene was amplified and visualized by agarose gel electrophoresis, as shown in Fig. 4d. There are no non-specific products and primer-dimers. The addition of PCR components such as primer, probe, and polymerase above the minimal concentration produces undesirable results, for instance, false-positive/false-negative results and/or insufficient PCR amplification. The combination of primer and polymerase concentrations that yielded optimal assay performance was chosen for further microfluidic PCR tests (500 nM of probe and 2.5 units of polymerase), as shown in Fig. 4e and f.

As a next step, bubble-free microfluidic PCR with a rapid Peltier-based thermal cycler system was performed in a run time of 2 min 10 s (35 PCR cycles, no hold time, single cycle: 3.7 s) with denaturation at 94 °C for 0 s and annealing/extension at 59 °C for 0 s, as shown in Fig. 4g and h. The PCR sample with a copy number at 3.75×10^3 copies/1 μl (see the Experimental Section for more details) was loaded into the reaction chambers of microfluidic PCR chip and DNA amplification was performed. This system maintains a high heating rate of greater than 35.9 ± 2.9 °C/s and a cooling rate of 12.6 ± 0.4 °C/s. After running 35 cycles, we evaluated the results with end point fluorescence analysis. Successful amplification with good signal-to-noise ratio (SNR 2.5:1) is shown in Fig. 4i. After rapid microfluidic PCR cycle with two-step amplification, the fluorescence intensity of PCR amplicons in the PCR chambers was clearly distinguishable under the small volumes of microfluidic PCR conditions. However, the weak fluorescence intensity from the microfluidic PCR amplification was observed due to the lower amplification efficiency compared to a benchtop thermocycler. The limit of detection in the microfluidic PCR is calculated to be 75 copies/single PCR well, which corresponds in terms of copy number of 15 cells (mean cMET copy number ≈ 5 copies/each NSCLS cell)(Cappuzzo et al., 2009; Engelman et al., 2007; Steen et al., 2015). The limit of quantification was determined to be 247 copies/single PCR well with $R^2 = 0.98$. The precision represented by coefficient of variation (CV) was determined to be 11.1%. The PCR amplification about tens of copies/reaction well is feasible in our microfluidic PCR system. Remarkably, the total amplification time in microfluidic PCR (2 min 10 Section, < 3 min) was approximately 20-fold faster than benchtop qPCR of approximately 60 min. In general, shortened PCR thermal cycling resulted in low PCR amplification yield, but it is possible to amplify the target amplicon up to 500 bp in length for less than 5 min under singleplex PCR (Houssin et al., 2016; Maltezos et al., 2010; Wheeler et al., 2011).

4. Conclusion

We have presented a rapid microfluidic NA diagnostic platform capable of producing a reliable bubble-free microfluidic PCR. Our approach for the bubble-free microfluidic PCR via a PE liquid/gas barrier is highly suitable for liquid handling with the largely minimized fluid loss. Compared to previously reported microfluidic PCR (BaTrung et al., 2010), our approach offers the advantages, including 1) fast time to results (< about 3 min), 2) guideline for efficient bubble-free PCR chamber design, allowing the guided-fluid transport as well as the pumpless sample injection, and 3) format flexibility for on-site POC testing along with a fabrication convenience. Consequently, the bubble-free functionality through the PE-PDMS hybrid structure and the efficient design of the PCR chamber effectively reduce the bubble generation and liquid loss. Finally, successful amplification of *cMET*, a lung cancer biomarker gene, was executed using the bubble-free microfluidic PCR. As an outlook, it is important to further optimize the contributing PCR parameters to maintain analytical specificity and PCR efficiency ragarding shorter thermal cycling. To match the faster cycling speed, the considerations regarding primer redesign by adding more bases, the highest possible annealing temperature, the use of a specialized rapid polymerase, final extension time, number of cycles, and a well-optimized PCR formulation including primer/probes and polymerase may be necessary. Therefore, the rapid microfluidic PCR system presented here has great potential as a simple use, rapid NA detection platform in a variety of diagnostic fields such as timely diagnosis of acute infectious and cardiac diseases, and rapid bio-warfare at the POC level.

Acknowledgements

This work was supported by the Bill and Melinda Gates Foundation through the Grand Challenges in Global Health Initiative OPP1028785, the Defence Advanced Research Projects Agency (DARPA) HR0011-12-2-0003, and the Mid-Career Researcher Support Program of National Research Foundation of Korea (NRF) by the Ministry of Science, ICT, and Future Planning (MSIP) (No. 2016R1A2B3014157).

Conflict of interest

The authors declare that they no conflict of interest.

Appendix A. Supporting information

Supplementary data associated with this article can be found in the online version at doi:10.1016/j.bios.2018.10.005.

References

Almassian, D.R., Cockrell, L.M., Nelson, W.M., 2013. Chem. Soc. Rev. 42, 8769–8798.
BaTrung, N., Saito, M., Takabayashi, H., Viet, P.H., Tamiya, E., Takamura, Y., 2010. Sens. Actuators B 149, 284–290.
Blume, I., Schwering, P.J.F., Mulder, M.H.V., Smolders, C.A., 1991. J. Membr. Sci. 61, 85–97.
Boone, T.D., Fan, Z.H., Hooper, H.H., Ricco, A.J., Tan, H., Williams, S.J., 2002. Anal. Chem. 74, 78–86.
Bustin, S.A., Benes, V., Garson, J.A., Hellemans, J., Huggett, J., Kubista, M., Mueller, R., Nolan, T., Pfaffl, M.W., Shipley, G.L., Vandesompele, J., Wittwer, C.T., 2009. Clin. Chem. 55, 611–622.
Cappuzzo, F., Marchetti, A., Skokan, M., Rossi, E., Gajapathy, S., Felicioni, L., Grammastro, Md, Sciarrotta, M.G., Buttitta, F., Incarbone, M., Toschi, L., Finocchiaro, G., Destro, A., Terracciano, L., Roncalli, M., Alloisio, M., Santoro, A., Varella-Garcia, M., 2009. J. Clin. Oncol. 27, 1667–1674.
Dimov, I.K., Basabe-Desmonts, L., Garcia-Cordero, J.L., Ross, B.M., Ricco, A.J., Lee, L.P., 2011. Lab Chip 11, 845–850.
Engelman, J.A., Zejnullahu, K., Mitsudomi, T., Song, Y., Hyland, C., Park, J.O., Lindeman, N., Gale, C.-M., Zhao, X., Christensen, J., Kosaka, T., Holmes, A.J., Rogers, A.M., Cappuzzo, F., Mok, T., Lee, C., Johnson, B.E., Cantley, L.C., Jänne, P.A., 2007. Science 316, 1039–1043.
Farrar, J.S., Wittwer, C.T., 2015. Clin. Chem. 61, 145–153.
Heyries, K.A., Tropini, C., VanInsberghe, M., Doolin, C., Petriv, O.I., Singhal, A., Leung, K., Hughesman, C.B., Hansen, C.L., 2011. Nat. Methods 8, 649–651.
Hung, T.Q., Chin, W.H., Sun, Y., Wolff, A., Bang, D.D., 2017. Biosens. Bioelectron. 90, 217–223.
Houssin, T., Cramer, J., Grojsman, R., Bellahsene, L., Colas, G., Moulet, H., Minnella, W., Pannetier, C., Leberre, M., Plecis, A., Chen, Y., 2016. Lab Chip 16, 1401–1411.
Jiang, L., Mancuso, M., Lu, Z., Akar, G., Cesarman, E., Erickson, D., 2014. Sci. Rep. 4, 4137.
Karlsson, J.M., Gazin, M., Laakso, S., Haraldsson, T., Malhotra-Kumar, S., Mäki, M., Goossens, H., Wijngaart, W. vd, 2013. Lab Chip 2013, 4366–4373.
Lee, S.H., Kwon, O.S., Song, H.S., Park, S.J., Sung, J.H., Jang, J., Park, T.H., 2012. Biomaterials 33, 1722–1729.
Liao, C.-S., Lee, G.-B., Liu, H.-S., Hsieh, T.-M., Luo, C.-H., 2005. Nucleic Acids Res. 33, e156.
Liao, Y., Wang, X., Sha, C., Xia, Z., Huang, Q., Li, Q., 2013. Nucleic Acids Res. 41, e76.
Liu, H.-B., Gong, H.-Q., Ramalingam, N., Jiang, Y., Dai, C.-C., Hui, K.M., 2007. J. Micromech. Microeng. 17, 2055–2064.
Liu, J., Fu, H., Yang, T., Li, S., 2015. Biomicrofluidics 9, 054118.

Liu, W., Zhang, M., Liu, X., Sharma, A., Ding, X., 2017. Biosens. Bioelectron. 96, 213–219.
Ma, Y.-D., Chang, W.-H., Luo, K., Wang, C.-H., Liu, S.-Y., Yen, W.-H., Lee, G.-B., 2018. Biosens. Bioelectron. 99, 547–554.
Maltezos, G., Gomez, A., Zhong, J., Gomez, F.A., Scherer, A., 2008. Appl. Phys. Lett. 93, 243901.
Maltezos, G., Johnson, M., Taganov, K., Srichantaratsamee, C., Gorman, J., Baltimore, D., Chantratita, W., Scherer, A., 2010. Appl. Phys. Lett. 97, 264101.
Merkel, T.C., Bondar, V.I., Nagai, K., Freeman, B.D., Pinnau, I., 2000. J. Polym. Sci. Part B Polym. Phys. 38, 415–434.
Nakayama, T., Hiep, H.M., Furui, S., Yonezawa, Y., Saito, M., Takamura, Y., Tamiya, E., 2010. Anal. Bioanal. Chem. 396, 457–464.
Park, S.-m., Lee, J.Y., Hong, S., Lee, S.H., Dimov, I.K., Lee, H., Suh, S., Pan, Q., Li, K., Wu, A.M., Mumenthaler, S.M., Mallick, P., Lee, L.P., 2016. Lab Chip 16, 3682–3688.
Prakash, A.R., Adamia, S., Sieben, V., Pilarski, P., Pilarski, L.M., Backhouse, C.J., 2006. Sens. Actuators B 113, 398–409.
Rissin, D.M., Kan, C.W., Campbell, T.G., Howes, S.C., Fournier, D.R., Song, L., Piech, T., Patel, P.P., Chang, L., Rivnak, A.J., Ferrell, E.P., Randall, J.D., Provuncher, G.K., Walt, D.R., Duffy, D.C., 2010. Nat. Biotechnol. 61, 145–153.
Sayad, A., Ibrahim, F., Uddin, S.M., Cho, J., Madou, M., LinThong, K., 2018. Biosens. Bioelectron. 100, 96–104.
Shin, Y.S., Cho, K., Lim, S.H., Chung, S., Park, S.-J., Chung, C., Han, D.-C., Chang, J.K., 2003. J. Micromech. Microeng. 13, 768–774.
Shrivastava, A., Gupta, V.B., 2011. Chron. Young Sci. 2, 21–25.
Steen, N.V.D., Pauwels, P., Gil-Bazo, I., Castañon, E., Raez, L., Cappuzzo, F., Rolfo, C., 2015. Cancers 7, 556–573.
Ueberfeld, J., McKenna, B., Rubin-Bejerano, I., Verstrepen, K., Ehrlich, D.J., 2008. Anal. Chem. 80, 7430–7436.
Wheeler, E.K., Hara, C.A., Frank, J., Deotte, J., Hall, S.B., Benett, W., Spadaccini, C., Beer, N.R., 2011. Analyst 136 (3707-3702).
Xu, J., Vaillant, R., Attinger, D., 2010. Microfluid. Nanofluid. 2010, 765–772.
Xu, L., Lee, H., Jetta, D., Oh, K.W., 2015. Lab Chip 15, 3962–3979.
Yeh, E.-C., Fu, C.-C., Hu, L., Thakur, R., Feng, J., Lee, L.P., 2017. Sci. Adv. 3, e1501645.
Zhang, C., Xing, D., 2007. Nucleic Acids Res. 35, 4223–4237.
Zhang, C., Xu, J., Ma, W., Zheng, W., 2006. Biotechnol. Adv. 24, 243–284.